EES Solar

PAPER

View Article Online
View Journal

Check for updates

Cite this: DOI: 10.1039/d5el00177c

Chemical maximum-power-point tracking system for stabilized liquid solar-fuel production

Yasuo Matsubara, *[a] Hinako Kawakami,[b] Yasuhito Kajita[b] and Yutaka Amao [a]

Electrochemical production of fuels from solar energy, commonly referred to as solar-fuel production, is a key technology for converting abundant yet intermittent solar energy into a stable energy source. Typically, this process employs an electrolyzer coupled with photovoltaic (PV) cells through an electronic maximum power point tracking (MPPT) system. Here, we propose a chemical MPPT system, integrated directly into the electrolyzer, to enable stand-alone and unmanned liquid solar-fuel production with stabilized concentration changes from sunrise to sunset. The working principle of the MPPT system is derived from the impedance and heat-transfer properties of the electrolyzer, which incorporates a solid-state electrolyte exhibiting ionic resistivity with a negative temperature coefficient. Application of the mathematical model to a real electrolyzer energized by a commercially-available monocrystalline-Si PV panel for producing pure aqueous formic-acid solution demonstrated a high utilization factor (85%) of PV energy and a 2% external solar-to-formic-acid (eSTF) energy efficiency for 0.1 kg of formic acid from pure water and carbon dioxide (CO_2) during daytime operation, all without the use of a conventional electronic MPPT system.

Received 24th October 2025
Accepted 19th March 2026

DOI: 10.1039/d5el00177c

rsc.li/EESSolar

Open Access Article. Published on 20 March 2026. Downloaded on 4/10/2026 3:06:36 PM.
This article is licensed under a Creative Commons Attribution-NonCommercial 3.0 Unported Licence.

Broader context

Solar-fuel production is a key technology for harvesting solar energy—an abundant but intermittent resource with low flux density, into concentrated and persistent chemicals. The combination of an electrolyzer and a photovoltaic (PV) cell, aided by an electrical maximum-power-point tracking (MPPT) system, is a promising approach for realizing an autonomous artificial-photosynthetic machine to harvest solar energy in the form of chemical feedstocks. However, conventional MPPT systems, which require an expensive battery, present a fundamental contradiction: the goal is to produce solar fuel inexpensively, yet the system relies on a costly component. We propose that this contradiction can be resolved by eliminating redundancy, specifically the coexistence of two energy storage chemistries (battery and fuel) within the system. This proposal was theoretically supported by modeling an electrolyzer in terms of heat and electricity; the maximum power-point of a PV cell was found to be trackable by the electrolyzer under certain conditions. We also demonstrated this self-regulating approach using our stand-alone, unmanned machine energized by a commercially available PV panel for producing pure aqueous formic-acid solution from CO_2 and pure water in stabilized concentration (3 wt%) with 2% external energy efficiency during daylight. This marks a milestone on the path to a human-made photosynthetic machine.

Introduction

Stabilization of concentration, purity, and efficiency in continuous liquid solar-fuel production is essential for such industrial applications that rely on solar energy, which is abundant but intermittent and characterized by low flux density. However, in the promising case of an electrolyzer powered by a photovoltaic (PV) cell,[1,2] two limitations of solar energy must be addressed to achieve stabilization: (1) solar irradiance, which strongly depends on weather and climate conditions, governs the rate of the power-to-chemical process (concentration issue); and (2) the existence of a maximum power point in the *I–V* characteristics of a PV cell (efficiency issue). An electronic maximum power point tracking (MPPT) system is usually employed to address these shortcomings and typically consists of an MPPT controller, a battery, and a DC–DC converter (Fig. 1). Although such systems are well known, their introduction increases redundancy, since both the electrolyzer and the battery serve as

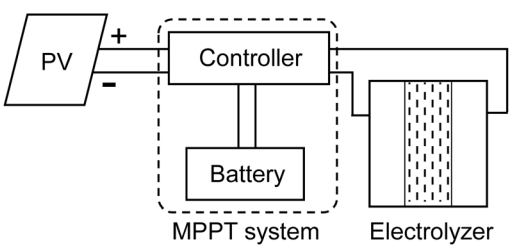

Fig. 1 Schematic configuration of a typical electrolyzer for solar-fuel production utilizing a conventional (electronic) MPPT system.

[a]Research Center for Artificial Photosynthesis, Osaka Metropolitan University, 3-3-138 Sugimoto, Osaka 558-8585, Japan. E-mail: yasuo@omu.ac.jp
[b]Advanced Technology Development Office, Iida Group Holdings Co., Ltd., 1-2-11 Nishikubo, Musashino-shi, Tokyo 180-0013, Japan

© 2026 The Author(s). Published by the Royal Society of Chemistry

Open Access Article. Published on 20 March 2026. Downloaded on 4/10/2026 3:06:36 PM.
This article is licensed under a Creative Commons Attribution-NonCommercial 3.0 Unported Licence.

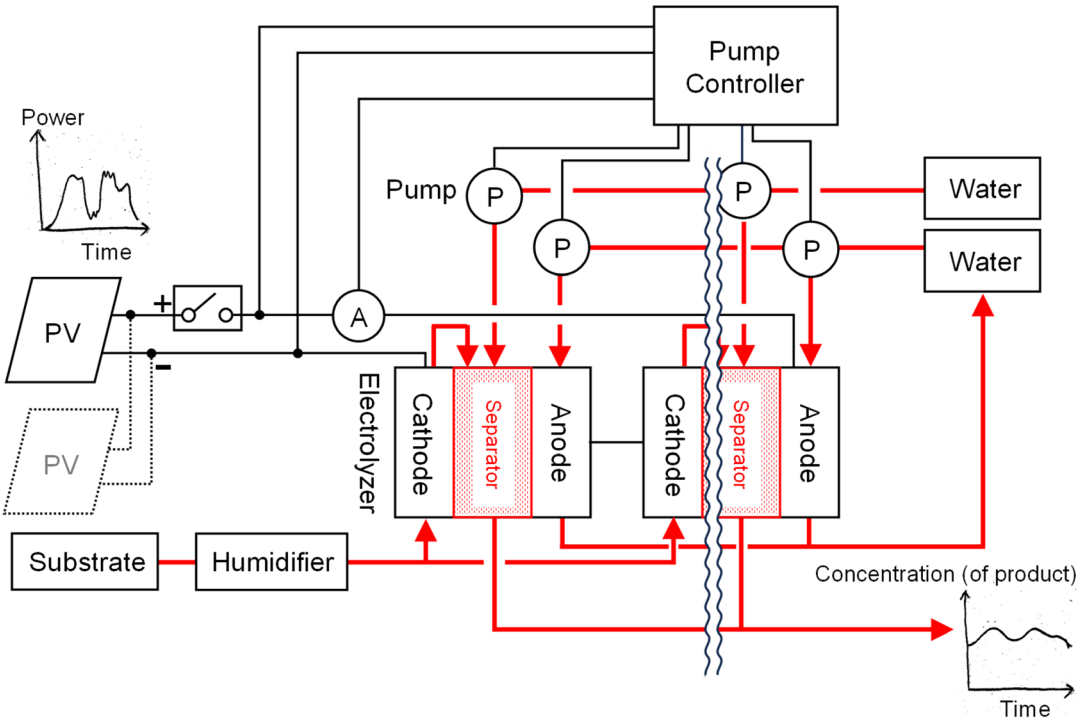

Fig. 2 Schematic configuration of the device proposed in this study. Symbols A and P denote an ammeter and a low-power-consumption pump, respectively. Electric wires and flow lines of water or substrate are represented by thin and bold lines, respectively.

solar-energy storage devices, and it also raises overall system cost. Alternatively, methods have been proposed that match the maximum power point (MPP) characteristics of a PV cell with the *I*–*V* properties of an electrolyzer, thereby eliminating the redundancy inherent in a conventional MPPT system.[3–7] However, these approaches cannot resolve the concentration issue and rely on costly *a priori* customization of the physical properties of the PV cell and/or electrolyzer.

Here, we propose a yet another MPPT system integrated directly into an electrolyzer for a stand-alone device performing stabilized liquid solar-fuel production, as illustrated in Fig. 2. The electrolyzer consists of three compartments: (1) an anode chamber, (2) a cathode chamber, and (3) a separator composed of a solid-state electrolyte (SSE, *e.g.*, ion-exchange resin), which exhibits ionic resistivity with a negative temperature coefficient (NTC), meaning its ionic conductivity increases with temperature. If the anode and/or cathode materials contain SSE, a similar temperature effect can be observed, as discussed later. The series of electrolyzers is directly connected to the PV cell. A pump controller monitors the current through the electrolyzers and regulates the flow rates of water and/or substrate using low-power-consumption pumps that transfer water and/or substrate from a reservoir to the electrolyzers. The electrolyzers begin production at sunrise and stop at sunset. This chemical MPPT system enables near-constant liquid solar-fuel concentrations without the need for a conventional MPPT system or a custom-designed PV cell.

Results and discussion

Theoretical model of the chemical MPPT system

The working principle of the MPPT function in this device is based on the ionic resistivity of the SSE and the thermal dissipation from the electrolyzer, which is regulated by the flow rates of water through the respective pumps. At room temperature, the ionic conductance of the SSE is typically too low to efficiently utilize the energy generated by the PV cell. In contrast, at elevated temperatures caused by self-heating, the conductance increases sufficiently to allow a large current to pass through the electrolyzer. The working point on the *I*–*V* curve of the electrolyzer is regulated by controlling thermal dissipation *a posteriori* to match the MPP of the PV cell under real-time weather conditions; that is, low and high flow rates are applied under low and high solar irradiance, respectively. This behavior also results in the averaging of the concentration of the chemical product. In the following section, theoretical models of the electrolyzer system are described in terms of impedance and heat transfer.

Impedance model. Fig. 3 shows an impedance model of the electrolyzer system, in which an electrolyzer is directly connected to a PV cell. The current, I (and voltage, V), is monitored by a pump controller that regulates the flow rate of substrates (*e.g.*, water) from the reservoir. The apparent resistance of the operating electrolyzer can be divided into three components: the resistance of the cathode chamber (R_c), the SSE separator (R_s), and the anode chamber (R_a). Note that this model does not include any capacitance, as the system is analyzed in the low-

© 2026 The Author(s). Published by the Royal Society of Chemistry

Open Access Article. Published on 20 March 2026. Downloaded on 4/10/2026 3:06:36 PM.
This article is licensed under a Creative Commons Attribution-NonCommercial 3.0 Unported Licence.

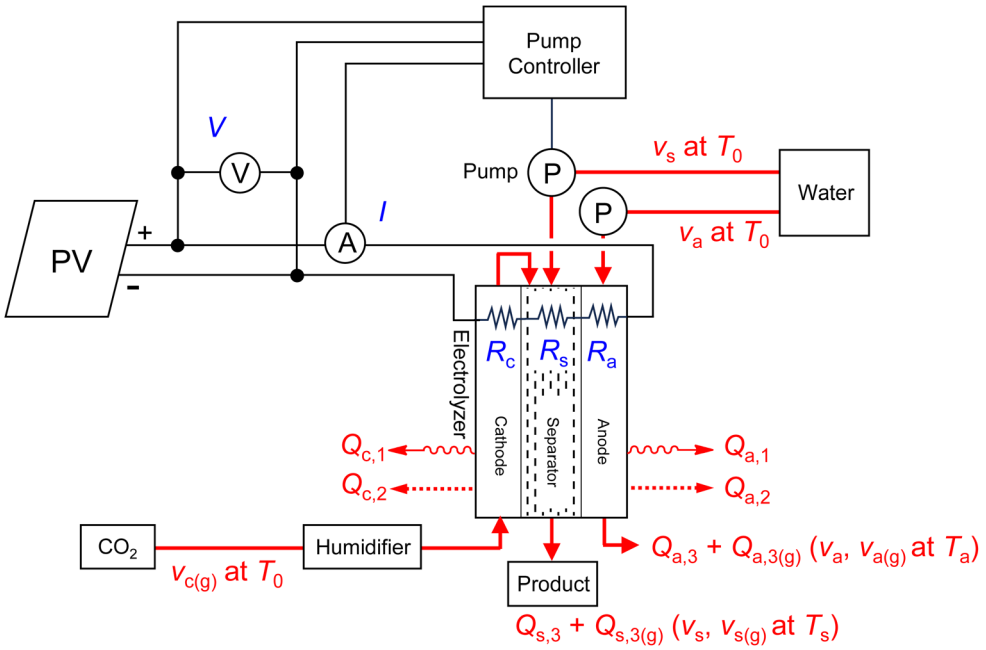

Fig. 3 Impedance and thermal models of the proposed system, consisting of an electrolyzer with a solid-state electrolyte (SSE) as the separator. Symbols denote resistances (R_i), the voltage of the PV cell (V), the current passing through the electrolyzer (I), flow rates (v_i for liquid and $v_{i(g)}$ for gas), temperatures of fluids (T_i), and amounts of heat transfer by the fluid *via* advection mechanism ($Q_{i,3}$ for liquid and $Q_{i,3(g)}$ for gas) and from a surface ($Q_{i,1}$ by radiation and $Q_{i,2}$ by convection). Units are expressed in Ω, V, A, mL min^{-1}, K, W, and W, respectively, where the subscript "i" indicates the relevant compartment (*e.g.*, a = anode chamber; c = cathode chamber; and s = separator).

frequency limit. The resistance R_s can be further separated into temperature-dependent and temperature-independent terms ($R_{s,Ts}$ and $R_{s,0}$, respectively). The former is estimated using the quotient of two Arrhenius equations with a single activation energy for ionic conduction, $E_{a,s}$ (eqn (1)), although the porous-plug model for three potential conduction paths has also been established.[8–11] In this equation, T_s and T_0 are the temperatures of water flowing out of and into the electrolyzer, respectively; k_B is the Boltzmann constant; and $R_{s,Ts}$ and $R_{s,T0}$ are the resistances of the SSE separator at T_s and T_0, respectively—that is, the temperature of the SSE separator is assumed to be equal to that of the water flowing out. The current, I, is calculated using eqn (2) in the form of the Tafel equation, under the assumption that only the cathodic reaction limits the current passing through the electrolyzer. Here, F is the Faraday constant; α is the charge-transfer coefficient, assumed to be 0.5 in this study; R is the gas constant; and $k_{app,T0,i}$, $E_{cat.i}$, and n_i are the apparent rate constant, the sum of onset potentials of the catalysts, and the number of electrons involved in the net reaction proceeding in the electrolyzer, respectively (the subscript "i" indicates the type of reaction). $E_{a,TPB,i}$ is assumed to be the activation energy at the three-phase boundary of the electrocatalyst, SSE ionomer, and substrates (liquid and gas) existing in proximity to the SSE separator.

$$R_s = R_{s,T_s} + R_{s,0} = R_{s,T_0} e^{\frac{E_{a,s}}{k_B}\left(\frac{1}{T_s} - \frac{1}{T_0}\right)} + R_{s,0} \quad (1)$$

$$I = \frac{V - IR_s}{R_c + R_a} = F\sum_i n_i k_{app,T_0,i} e^{-\frac{E_{a,TPB,i}}{k_B}\left(\frac{1}{T_s} - \frac{1}{T_0}\right)} e^{\frac{\alpha F}{RT_s}(V - IR_s - E_{cat,i})} \quad (2)$$

Thermal model. Fig. 3 also presents a thermal model of the system, in which the electrolyzer transfers heat to the surroundings *via*: (1) radiation from the surfaces of the anode and cathode chambers ($Q_{a,1}$ and $Q_{c,1}$, respectively); (2) convection of air on the surfaces of the anode and cathode chambers ($Q_{a,2}$ and $Q_{c,2}$, respectively); and (3) advection ($Q_{a,3}$ and $Q_{s,3}$) induced by the flow of water at rates v_a and v_s, respectively.[12] For the electrolyzer examined in this study, we found that, within the current range below approximately 10 A (0.4 A cm^{-2}): (1) the sum of the estimated heat transfers ($Q_{cell(est)}$ in eqn (3a)) is nearly equal to the power consumed by the electrolyzer (Q_{cell} in eqn (3b)), except for the contributions from the enthalpy changes ($\Delta_f H_i$) of the two electrode reactions proceeding in the electrolyzer with faradaic efficiencies (FE_i); and (2) the heat transfer due to radiation, which is proportional to T^4, is much smaller than that due to convection and advection, which are proportional to $T^{1.25}$ and T^1, respectively, *i.e.*, $Q_{a,1} + Q_{c,1} << Q_{a,2} + Q_{c,2} + Q_{a,3} + Q_{s,3}$ (see Fig. S2 in Section B of the SI). We therefore approximate Q_{cell} as a function of T_s, the characteristic temperature of the electrolyzer, with a thermal dissipation constant δ (in units of W K^{-1}), as expressed in eqn (3b). We also found that vaporization and boiling ($Q_{s,3(g)}$ and $Q_{a,3(g)}$) play an important role in transferring a large amount of heat to the

Open Access Article. Published on 20 March 2026. Downloaded on 4/10/2026 3:06:36 PM.
This article is licensed under a Creative Commons Attribution-NonCommercial 3.0 Unported Licence.

surroundings of the electrolyzer when the current exceeds approximately 10 A (0.4 A cm^{-2}) in our case. In this current range, the approximation in eqn (3b) is no longer valid for describing the thermal behavior of the electrolyzer. Interestingly, we found that this δ can be related to the sum of the flow rates, $v_a + v_s$, as described later.

$$Q_{cell(est)} = \sum_i \sum_j Q_{i,j} \tag{3a}$$

$$Q_{cell} = I\left(V - \sum_i FE_i \frac{\Delta_f H_i}{n_i F}\right) \approx \delta(T_s - T_0) \tag{3b}$$

Numerical simulation using the combined model. These equations contain the common temperature term, T_s. Eliminating this term from eqn (1) and (2) using eqn (4) yields a useful formula for analyzing the current–voltage (I–V) characteristics of an electrolyzer system containing SSE. Fig. 4 shows I–V curves (red lines) calculated by numerical simulation using eqn (2) and (4) for three values of δ (0.4, 0.5, and 0.6 W K^{-1}) as examples. The theoretical I–V curve (black line) for the MPPs of eight ideal c-Si cells in series at 25 °C, representing a PV array,[13] is also shown. In this case, a value of δ around 0.4 W K^{-1} appears to be optimal for receiving power from the PV cell with maximal utilization factor (UF), although the concentration of the product must also be taken into account.

$$T_s = I\left(V - \sum_i FE_i \frac{\Delta_f H_i}{n_i F}\right) \Big/ \delta + T_0 \tag{4}$$

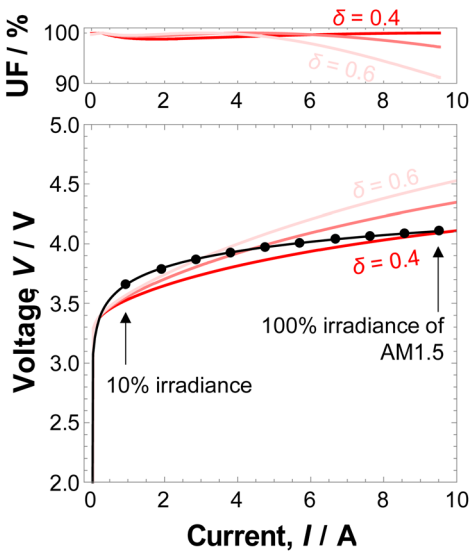

Fig. 4 Example of I–V curves (red lines) of the electrolyzer and utilization factors (UFs) of PV energy calculated by numerical simulation using eqn (1), (2) and (4) with three different values of δ (0.4, 0.5, and 0.6 W K^{-1}), while other parameters are held constant. The theoretical I–V curve for the MPPs of eight ideal c-Si cells at 25 °C in series as a PV array is shown as a black line, with black discs representing the I–V points of the MPPs at 0–100% (10% intervals) of the AM1.5 solar irradiance. See Section E of the SI for details.

The product concentration is proportional to the power, P, received from the PV array divided by the water flow rate in the SSE separator, v_s, provided that both the faradaic efficiency and the selectivity of the production are constant (eqn (5)). If we assume a relationship as expressed in eqn (6) with arbitrary parameters r and s, substitution of eqn (5) into eqn (6) yields eqn (7). This equation is useful for regulating the product concentration under variations in solar irradiance, as numerically simulated in Fig. 5. In the case of $s = 0.0$, the concentration is almost proportional to the power, which corresponds to the conventional situation. In contrast, when $s = 1.0$, the concentration is nearly invariant with respect to the power, as it becomes proportional to the voltage of the electrolyzer. This result indicates that the concentration can remain stable against changes in solar irradiance, while the utilization factor of the PV array can be optimized by selecting an appropriate flow rate (*e.g.*, eqn (6)).

$$c \propto P/v_s \tag{5}$$

$$v_s = r(I)^s \tag{6}$$

$$c \propto V \times I^{(1-s)} \tag{7}$$

Application of the theoretical model to a real electrolyzer system

For this model, we applied the system to the electrolyzer[14–18] to produce a pure aqueous formic acid solution without any added electrolyte, using carbon dioxide, pure water, and electricity generated by a PV array. In the following section, we describe how the single electrolyzer was characterized and the real electrolyzer system was build up.

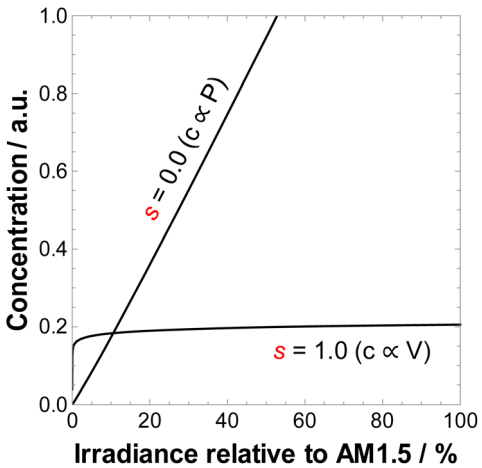

Fig. 5 Dependence of the product concentration on solar irradiance relative to AM1.5. The dependence was numerically calculated using eqn (7) for the cases of $s = 0.0$ and 1.0, where V and I were taken from the theoretical I–V curve for the MPPs of the PV array, as shown by the black line in Fig. 4. See Section E of the SI for details.

© 2026 The Author(s). Published by the Royal Society of Chemistry

Open Access Article. Published on 20 March 2026. Downloaded on 4/10/2026 3:06:36 PM.
This article is licensed under a Creative Commons Attribution-NonCommercial 3.0 Unported Licence.

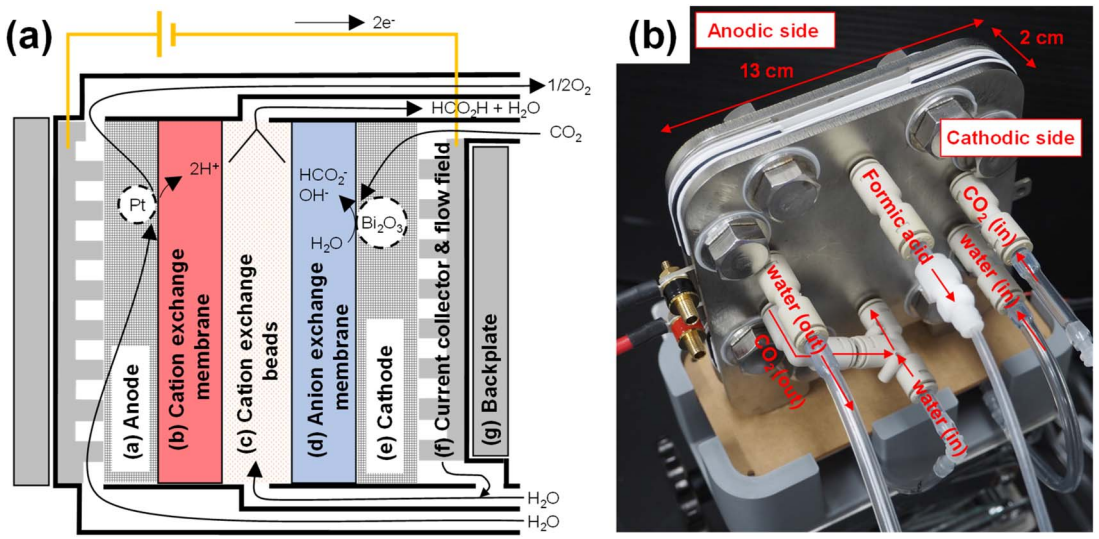

Fig. 6 (a) Schematic structure of the electrolyzer examined in this study. (b) Photograph of the assembled electrolyzer, with annotated flow lines of substrates and their directions. The geometric working area of the electrodes is 25 cm^2.

Step 1: single electrolyzer. The cell design was first reported by Masel's group[14,15] and later extended by Wang's group,[16,17] demonstrating that this cell architecture (illustrated in Fig. 6a) is capable of producing pure formic acid under certain conditions. The SSE discussed here is composed of a cation exchange membrane (b), beads made of cation exchange resin (c), and an anion exchange membrane (d) bridging the anode and cathode electrodes (a and e, respectively) on current collectors (f), with flow fields for water and carbon dioxide gas (CO_2). The beads act as the reaction field to produce formic acid through the neutralization of proton and formate generated in the anodic and cathodic reactions, in which water is oxidized to dioxygen and CO_2 is reduced to formate, respectively. In our laboratory, we confirmed that the electrolyzer shown in Fig. 6b, configured according to this cell architecture, produces a pure aqueous formic acid solution (6 wt%) at 10 A and a water flow rate of 1.5 mL min^{-1} (*i.e.*, approximately 113 g of acid produced over 24 hours with a faradaic efficiency of 63%).

Reaction stoichiometry and CO_2 atom-efficiency. According to previous reports, the ideal stoichiometry is assumed as represented in Fig. 6a. However, significant amounts of dihydrogen and carbon monoxide gases are also produced as byproducts, depending on the reaction conditions. Through thermal measurements using the electrolyzer (described below), we observed that: (1) the sum of faradaic efficiencies for the production of formic acid, dihydrogen gas, and carbon monoxide gas (97 ± 3%), and the efficiency for the production of dioxygen gas (95 ± 5%) are both close to 100% relative to the number of electrons passing through the system (see Table S1 (entries 1–11) in Section B of the SI); (2) one equivalent of water is consumed for the production of one equivalent (±5%) of the total amount of formic acid, dihydrogen gas, and carbon monoxide gas (see Section G of the SI); (3) the efficiency of formic acid production reaches a plateau (50–70%) at a CO_2 flow rate ($v_{c(g)}$) corresponding to approximately twice the amount of formic acid produced (see Fig. S1 in Section B of the SI); and (4) the ratio of the flux of CO_2 migration normal to the surface of the anion membrane to the bulk CO_2 flux ($v_{c(g)}$) is negligible (~1%; see Table S1 (entries 9 and 24) in Section B of the SI). These observations confirm that the reactions related to formic acid production in the electrolyzer are stoichiometrically represented by Fig. 6a, although the CO_2 atom efficiency is kinetically limited to around 50% likely caused by a large Thiele modulus.[19,20]

Thermal property. For the electrolyzer operating at fixed currents with various total water flow rates ($v_a + v_s$), we investigated the contributions of three types of heat transfer (see Section B of the SI). Fig. 7a shows the measured relationship between $Q_{cell(est)}$ with Q_{cell}, which were calculated using eqn (3a) and (3b), respectively. The linear relationship, with a slope of 0.94 close to unity, indicates that eqn (3a) appropriately reflects the heat transfer occurring in the electrolyzer, as depicted in Fig. 3, where convection and advection account for the majority of heat transfer (*i.e.*, $Q_{a,2} + Q_{c,2} + Q_{a,3} + Q_{s,3} >> Q_{a,1} + Q_{c,1}$; see also Fig. S2 in Section B of the SI). Fig. 7b shows the measured values of δ calculated using eqn (3b) (black discs). We found that the thermal dissipation constant δ exhibits a linear relationship with the total water flow rate (eqn (8), where $a = 0.050$, $b = 1.0$, and $c = 0.37$). Although the relationship of δ to $v_a + v_s$ is generally unknown, this is the first reported example for this type of electrolyzer.

$$\delta = a(v_a + v_s)^b + c \quad (8)$$

***I–V* property.** Fig. 7c shows the *I–V* characteristics of the electrolyzer operating at various currents with two fixed total water flow rates ($v_a + v_s$), corresponding to $\delta = 0.60$ W K^{-1} (discs) and 1.04 W K^{-1} (circles). In the current range of 1–10 A, the faradaic efficiency for formic acid production was 70 ± 5% (see

Open Access Article. Published on 20 March 2026. Downloaded on 4/10/2026 3:06:36 PM.
This article is licensed under a Creative Commons Attribution-NonCommercial 3.0 Unported Licence.

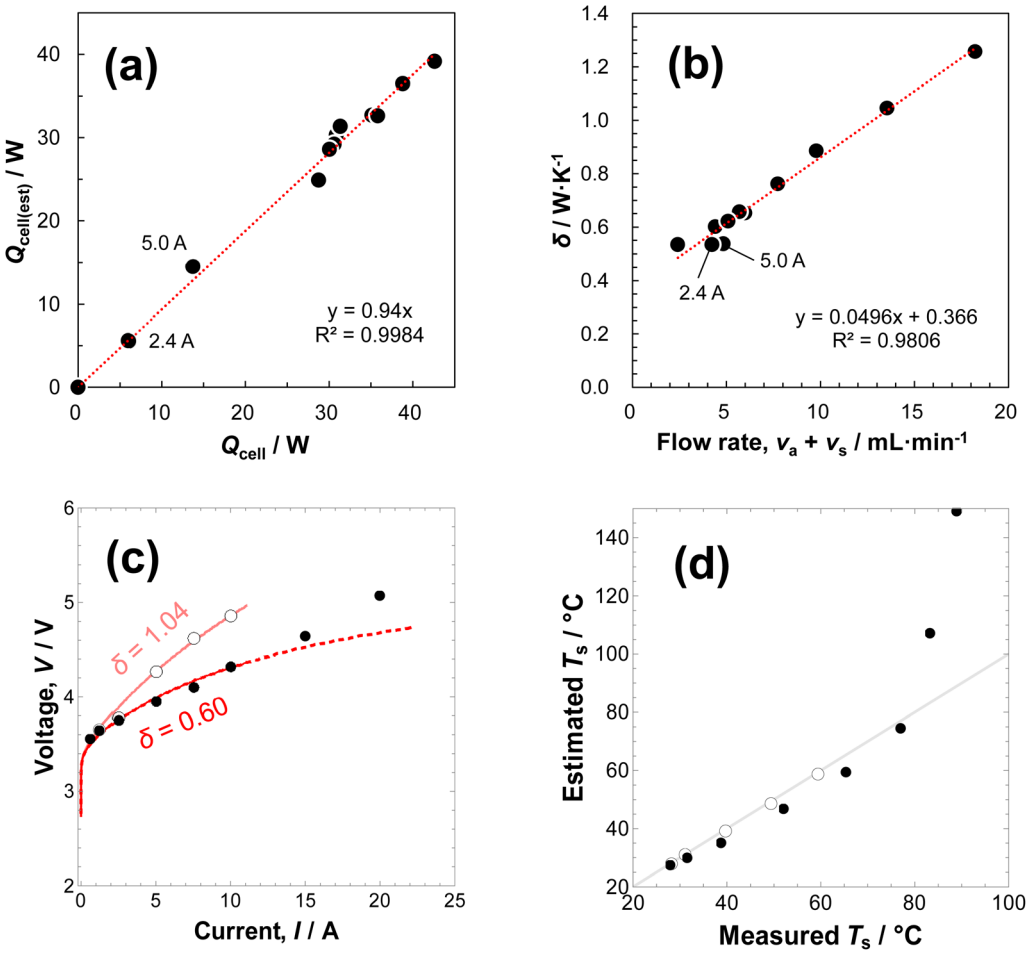

Fig. 7 (a) Correlation of Q_{cell} with $Q_{cell(est)}$ investigated using the electrolyzer operating at a fixed current (10 A unless otherwise noted) with various total flow rates, where $T_0 = 302 \pm 2$ K and $v_{c(g)} = 180 \pm 2$ sccm. (b) Linear relationship (dotted line) of the thermal dissipation constant, δ (disc), to the total flow rate, $v_a + v_s$, measured under the same conditions as in (a). The constant was calculated using eqn (3b). (c) I–V properties measured for the electrolyzer operating at various currents with two fixed total flow rates (4.7 and 13.5 mL min^{-1}), *i.e.*, $\delta = 0.60$ W K^{-1} (disc) and 1.04 W K^{-1} (circle), where $T_0 = 299 \pm 2$ K and $v_{c(g)}$ of CO_2 to be 180 ± 2 sccm (for $I \leq 10$ A) or 450 ± 5 sccm (for $I > 10$ A). CO_2 was humidified using a gas bubbler at room temperature (299 ± 2 K). Numerically fitted curves using eqn (2) and (4) are also shown (red and light-red curves for $\delta = 0.60$ and 1.04 W K^{-1}, respectively). See Section D of the SI for details of the fitting procedure. (d) Comparison of T_s estimated by eqn (4) with T_s measured under the same conditions as in (c).

Section H of the SI). At higher currents of 15 and 20 A, the faradaic efficiency decreased to 48 ± 5%, likely due to accelerated dihydrogen production as a side reaction. Numerical fitting using eqn (1), (2) and (4) (red curve) in the 1–10 A region adequately explains the observed I–V points. In this fitting, a single set of parameters was assumed for eqn (2): n (2), $k_{app,T0}$ (2.7×10^{-4} mol s^{-1}), $E_{a,TPB}$ (5.3 eV), and E_{cat} (3.6 V). For eqn (4), three sets of n, FE, and $\Delta_f H$ were used because the faradaic efficiencies of formic acid, dihydrogen gas, and carbon monoxide gas depended primarily on the flow rates v_a and v_s rather than the current density. $E_{a,s}$ of the SSE separator was determined separately (0.19 eV) using electrochemical impedance spectroscopy (EIS);[21] (see Section C of the SI for details). The small value of $R_{s,T0}$ (0.4 mΩ) indicates that the temperature dependence of the I–V curve ($\delta = 0.60$ and 1.04 W K^{-1}) is governed primarily by the large activation parameter $E_{a,TPB}$ (5.3 eV). The deviation of the fitted curve from the observed points at $I =$ 15 and 20 A is caused by an upward overestimation of T_s calculated from eqn (4) relative to the actual T_s, as shown in Fig. 7d (line). This discrepancy arises because we observed a visual transition from slug flow (at $I \sim 10$ A) to annular flow (at $I > 10$ A) of the product solution at the outlet of the SSE separator. Annular flow typically results from boiling phenomena and transfers a much larger amount of heat than forced advection without boiling.[22]

Step 2: multiple electrolyzers in series connected to a PV-array panel. Based on the analysis in Step 1, we constructed a stand-alone, unmanned device consisting of four electrolyzers (as used in Step 1) connected in series, as shown in Fig. 8. The schematic configuration of the device is illustrated in Fig. 2. The length and diameter of the electrical wire connecting the commercially-available monocrystalline-Si PV-array panels to the breaker box are 10 m each way per PV panel and nominally 3.5 mm^2, respectively, corresponding to a resistance of 0.11 Ω.

© 2026 The Author(s). Published by the Royal Society of Chemistry

Open Access Article. Published on 20 March 2026. Downloaded on 4/10/2026 3:06:36 PM.
This article is licensed under a Creative Commons Attribution-NonCommercial 3.0 Unported Licence.

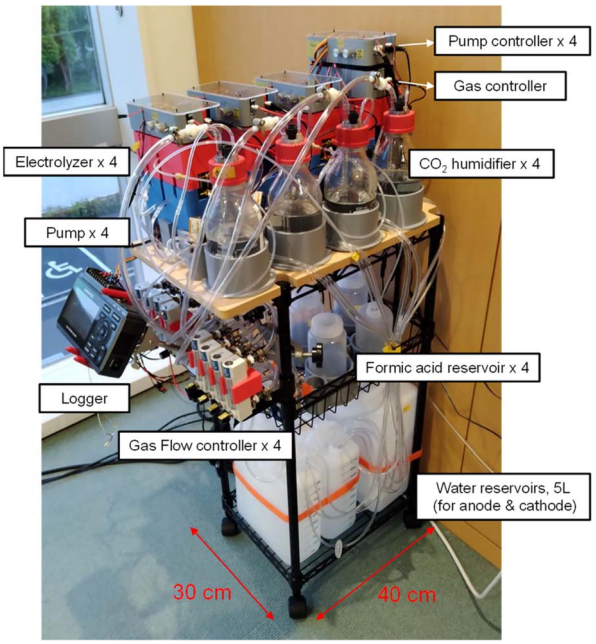

Fig. 8 Photograph of the stand-alone, unmanned device consisting of nine components, as annotated in the insets. The device initiates the production of formic acid solution simply by supplying CO_2 and electricity from external sources.

The resistances of the breaker box and the wiring between the electrolyzers and the box are 0.03 and 0.05 Ω, respectively. The device automatically starts production at sunrise and stops at sunset. It was confirmed to produce pure formic acid (approximately 3 wt% aqueous solution of 3.3 kg over a daylight period) with a purity greater than 98% from pure water, CO_2, and electricity directly supplied by the PV-array panel, as described below.

The device performance was examined on May 2, 2024, in Sugimoto, Osaka, Japan. The day was occasionally cloudy, as indicated by the changes in solar irradiance during the daylight period (see Fig. S6 in Section F of the SI). The thermal dissipation constant, δ, as a device parameter was set to $\delta = 0.010\ (I)^{1.0} + 0.54$, obtained from eqn (6) and (8), with the flow rate for the anode chamber, v_a, fixed at 3.5 mL min^{-1}, and the flow rate for the SSE separator, v_s, set to 0.2 $(I)^{1.0}$ mL min^{-1} (*i.e.*, $r = 0.2$ and $s = 1.0$ in eqn (6)) for the current range $I = 0$ to 20 A. Under these conditions, the simulated *I–V* curves of the four electrolyzers matched those of the PV cell used in this study by at least ~80% in terms of the utilization factor (UF) of PV energy (see Fig. S5 in Section E of the SI). Table 1 summarizes the observed performance of the device. We also tested the dependence of device performance on PV-array area, as indicated in column 2. As intended, relatively high UFs of the electricity generated by the PV-array (column 7; overall UF was 85%) and stable changes in the concentration of the formic acid solution (column 9) were observed throughout the daylight period, regardless of the absence of a conventional MPPT system. A closer examination of Table 1 reveals that (1) the UF before noon is lower than that after noon, and (2) the concentration in the early evening is relatively low compared with that at other times. The former is attributed to the non-ideal *I–V* behavior of the electrolyzer in the high-current region above 10 A (*i.e.*, the resistance of the electrolyzer increased beyond the value expected in Fig. 7a). The latter is attributed to operation under low solar irradiance, as indicated in Fig. 5. Nevertheless, a 2% external solar-to-formic-acid (eSTF) efficiency was achieved throughout the daylight period (column 11), which remains a state-of-the-art value to the best of our knowledge (see Section I of the SI for the definition of the eSTF). It should be noted that this value represents the net energy efficiency of the entire system, including energy consumption by peripheral devices (electrical pumps, controllers, and electrical wires; excluding the data logger). These results strongly support the utility of the present chemical MPPT system for stabilized solar-fuel production. Examination of the long-term performance of the device is ongoing. Evidently, the performance of this device solely depends on the durability of the electrolyzer and warrants to further research.

Experimental section

Chemicals

Water was purified using an ultrapure water purification system (Millipore, Direct-Q 5UV). XA-9 ionomer (Dioxide Materials, 5 wt% in ethanol), carbon black (Cabot, Vulcan XC-72R), Bi_2O_3 nanoparticles (US Research Nanomaterials, 99.9%, 80 nm), ethanol (Wako Pure Chemical, 99.5%), and potassium hydroxide (Wako Pure Chemical, 85.0%) were used as received. CO_2 gas (Nippon Sanso, 99.5%) was humidified using a simple gas-bubbler at room temperature immediately before entering the electrolyzer.

Apparatus

Formic acid produced in the solution during electrolysis was quantified using an ion chromatography system (Tosoh, IC-8100EX) with an anion-exchange column (Tosoh, TSKgel SuperIC-Anion HS) and a suppressor gel (Tosoh, TSKgel Suppress IC-A), employing an aqueous carbonate buffer solution (sodium bicarbonate, 7.5 mM and sodium carbonate, 0.8 mM) as the eluent. The gaseous reaction products—N_2, O_2, CO_2, CH_4, CO and H_2—were analyzed using a gas chromatograph (GL Sciences, GC-3210) equipped with a thermal conductivity detector (TCD) and an activated carbon column assembly (Molecular Sieves 13X, 3 m × 2.2 mm i.d.; Porapak T, 2 m × 2.2 mm i.d.; Porapak Q, 2 m × 2.2 mm i.d.). Electrochemical impedance spectroscopy (EIS) measurements were conducted using a potentiostat (BioLogic Scientific, VSP-300) with an airtight four-electrode electrochemical cell (Toyo, SH2-Z) placed in a thermostatic chamber (EYELA, LTI-2000C). The PV-array panel, made of monocrystalline Si (Choshu Industry, CS-223B83, the nominal illuminated area, A is 1.0 m^2), was mounted horizontally on our housetop and the temperature change of the panel was measured using a thermocouple attached to the backside of the panel. The *I–V* curve of the PV-array panel was recorded using an *I–V* curve tracer (Eiko, MP-11) where the contact resistance between the tracer and PV

Open Access Article. Published on 20 March 2026. Downloaded on 4/10/2026 3:06:36 PM. This article is licensed under a Creative Commons Attribution-NonCommercial 3.0 Unported Licence.

Table 1 Observed performance of the device, characterized by the geometric area of the PV array used (A); energy received by the PV array from sunlight (W_{sun}); maximal electricity that could be generated by the PV array ($W_{pv,mpp}$); energy received by the electrolyzers (W_{cell}); total energy consumed by peripherals, *i.e.*, the device controllers, pumps, and electrical wires ($W_{peripheral}$); estimated utilization factor (UF); volume (vol.) and concentration (c) of the produced aqueous formic acid solution; faradaic efficiency (FE) for the production; and external solar-to-formic-acid efficiency (eSTF) measured on May 2, 2024, at Sugimoto, Osaka, Japan

Time	A/m^2	W_{sun}/kWh	$W_{pv,mpp}$[a]/kWh	W_{cell}/kWh	$W_{peripheral}$/kWh	UF[b]/%	Vol./L	c/mol L^{-1}	FE/%	eSTF[c]/%
5:54–10:40	2.0	3.97	0.75	0.51	0.04	73	1.20	0.79	50	1.7
10:40–12:15	2.0	2.02	0.35	0.29	0.03	93	0.78	0.71	49	2.0
12:50–15:00	1.0	1.57	0.28	0.27	0.02	106	0.86	0.71	54	2.8
15:00–18:10	1.0	0.52	0.10	0.09	0.01	104	0.52	0.42	51	3.0

[a] See Section E in the SI for the calculation in detail. [b] Value calculated by $(W_{cell} + W_{peripheral})/W_{pv,mpp} \times 100$. [c] Value calculated by $-c \cdot \text{vol.} \cdot \Delta_c G^\circ / W_{sun} \times 100$ where the standard enthalpy of combustion of formic-acid (in aqueous solution) is adopted as the energy density of formic acid ($\Delta_c G^\circ = -258.1$ kJ mol; see Sections A and I of the SI).

panel was approximately 0.4 Ω. Solar irradiance was measured with a pyranometer mounted parallel to the PV-array panel (Eiko, ML-01, 39.8 μV (W^{-1} m^{-2})). The CO_2 gas flow rate, expressed in standard cubic centimeters per minute (sccm), was regulated using a mass flow controller (Kofloc, 3660-RC1/4-CO2-500SCCM-20 °C), where sccm in this study corresponds to the flow at 0 °C and 1 atm. Numerical fittings and simulation of the device performances were performed using a technical computing system (Wolfram Mathematica 10.0.1.0).

Preparation of electrodes

A gas-diffusion electrode for the cathode was prepared following procedures similar to those reported in previous literature.[14,15] The catalyst ink was prepared in two steps: (1) the addition of water (1.6 mL), ethanol (32 mL), and an ethanol solution (1.0 mL containing XA-9 ionomer at 5 wt%) to a mixture of Bi_2O_3 nanoparticles (600 mg) and Vulcan XC-72R carbon powder (600 mg); and (2) sonication of the mixture three times for 6 min each using an ultrasonic homogenizer (900 W). The resulting ink was air-brushed onto a carbon paper (10 × 10 cm; AvCarb MGL370, 50 wt% wet-proofed with PTFE) and dried at 120 °C under air. Typical Bi_2O_3 loading was 2.5–3.0 mg cm^{-2}. The paper was then cut into four square pieces (5 × 5 cm each). The sprayed side of each piece was soaked in an aqueous potassium hydroxide solution (1 M) for 3 h and dried at room temperature under air.

For the anode, a porous titanium-fiber sheet (thickness, 0.50 mm; porosity, 78%; Bekaert Currento 2GDL10N-050, coated with 0.2 μm platinum) was cut into 5 × 5 cm pieces, washed sequentially with hexane and acetone, and dried prior to use.

Assembly of the electrolyzer

The electrolyzer (structure depicted in Fig. 6 in the main text) was assembled in a three-compartment configuration as reported in the literature.[14,15] The electrolyzer comprised: (a) the porous titanium-fiber sheet described above for the anode, (b) a cation-exchange membrane—either Aquivion E98-15S (Syensqo) or Nafion 117 (Chemours), (c) a layer (t = 1.0 mm) packed with cation-exchange beads (Amberlite IRC120 H), (d) an anion-exchange membrane (Dioxide Materials Sustanion X37-FA), (e) the gas-diffusion electrode described above for the cathode, (f) two titanium current collectors with serpentine flow fields, and (g) two backplates. The cation-exchange membrane was soaked in pure water for three days prior to use. The cation-exchange beads were sieved to exclude beads with diameters greater than 0.6 mm and then soaked in an aqueous sulfuric acid solution (1 M) for three days before use. The anion-exchange membrane was pressed at 60 °C for 1 h and then soaked in an aqueous potassium hydroxide solution (1 M) for three days, with the solution replaced daily. These components were stacked in the order shown in Fig. 6 and tightened with eight sets of bolts and nuts to compress the layer of cation-exchange beads to approximately 1.0 MPa, as confirmed using three pressure-sensitive sheets (Fujifilm Prescale LW, LLW, and LLW). To activate the assembled electrolyzer, a constant voltage (*e.g.*, 6.0 V) was first applied until the current reached 10 A, after which a constant current (*e.g.*, 10 A) was applied until the voltage stabilized, under the following flow conditions: water flowing through the anode chamber at 3.2 mL min^{-1}, water flowing through the SSE separator at 1.5 mL min^{-1}, and CO_2 flowing through the cathode chamber at 180 sccm.

Assembly of the stand-alone and unmanned device

The device (structure depicted in Fig. 2 in the main text) was assembled with one or two PV-array panels (Choshu Industry, CS-223B83); a latching solenoid valve for gas control (Takasago Fluidic Systems, WLB-2K-N4F5); two water reservoirs; four sets of the electrolyzer; two low-power-consumption piezoelectric pumps (Takasago Fluidic Systems, APP-30WKG); a controller for the pumps (Takasago Fluidic Systems, MPD-200A); and a gas-bubbler at room temperature to humidify the CO_2 gas. The water flow rate from the pumps was automatically regulated by the pump controller, which received current information from the electrolyzer measured using a 1 mΩ shunt resistor. The sequence of actions of these components was organized by a low-power-consumption microprocessor (Microchip, PIC16F1778). The electricity for the pumps, pump controller, valve, and microprocessor was provided by a buck-boost DC/DC converter (Analog Devices, LTC3130-1) connected to the PV-array panel in parallel to electrolyzers. The total power

 © 2026 The Author(s). Published by the Royal Society of Chemistry

Open Access Article. Published on 20 March 2026. Downloaded on 4/10/2026 3:06:36 PM.
This article is licensed under a Creative Commons Attribution-NonCommercial 3.0 Unported Licence.

consumption (P_{ctrl}/W) of these 4 controllers and 8 pumps was rated as a function of the current (I/A) passing through the four electrolyzer in series ($0.05\ I + 1.0$).

Conclusion

In this study, we investigated the impedance and heat-transfer properties of an electrolyzer consisting of a solid-state electrolyte exhibiting ionic resistivity with a negative temperature coefficient and established the corresponding impedance and thermal models, as expressed in eqn (4). The combined model indicates that the thermal dissipation constant, δ, as a single parameter, is useful for adjusting the working point of the system to the maximum power point (MPP) of the PV cell, as shown in Fig. 4. In the case of the electrolyzer structure reported by Masel's group, the value of δ was found to follow eqn (8), where the total flow rate, $\nu_a + \nu_s$, of the substance (*i.e.*, water) exhibits a linear relationship with δ. This observation is crucial both for (1) stabilizing the product concentration, which is determined by fluctuating and intermittent solar power relative to the flow rate, as represented by eqn (5)–(7); and (2) simultaneously optimizing the utilization factor of the PV cell. The concentration can remain nearly invariant with respect to solar irradiance only when ν_s is a function of the current, I, to approximately the first power, as shown in Fig. 5. The utilization factor (UF) of the PV cell can be maximized by selecting an optimal value of δ that satisfies both eqn (6) and (8). These mechanisms can operate from sunrise to sunset because the I–V and irradiance–concentration curves are continuous functions, as shown in Fig. 4 and 5. We refer to these procedures as a chemical MPPT system. Application of the combined model confirmed (1) the stable concentration of the formic acid solution and (2) a relatively high utilization factor of energy from a commercially-available PV-array panel. These results represent an important milestone toward the practical realization of an electrolyzer system for stabilized liquid solar-fuel production.

Conflicts of interest

The authors have a Japan patent application (2024-124743) on the chemical MPPT system discussed here. H. K. and Y. K. are employees of Iida Group Holdings Co., Ltd.

Data availability

The data supporting this article have been included as part of the supplementary information (SI). Supplementary information: thermochemical quantities relevant to formic acid; observed thermal properties of the electrolyzer; EIS measurement of the separator; mathematical procedures and computing programs to calculate the theoretical I–V curve for the maximum-power-points of a PV array and the utilization factor of its energy; and observed time-course of solar-irradiance changes. See DOI: https://doi.org/10.1039/d5el00177c.

Acknowledgements

This work was funded by Iida Group Holdings Co., Ltd. We acknowledge the contributions of Miyuki Fujimura and Saori Muramoto in the assembly and testing of the electrolyzers. We also thank Hiroshi Hida, Atsushi Hirokawa, Manami Ito, Akinori Kitamura, Mako Kuwata, and Yasushi Sato for their valuable technical assistance. Y. M. is grateful to his wife, Kazuko, for her devoted support that made this contribution possible.

References

1 J. He and C. Janáky, Recent Advances in Solar-Driven Carbon Dioxide Conversion: Expectations *versus* Reality, *ACS Energy Lett.*, 2020, **5**, 1996–2014.
2 R. I. Masel, Z. Liu, H. Yang, J. J. Kaczur, D. Carrillo, S. Ren, D. Salvatore and C. P. Berlinguette, An industrial perspective on catalysts for low-temperature CO_2 electrolysis, *Nat. Nanotechnol.*, 2021, **16**, 118–128.
3 B. Thijs, L. Hanssens, G. Heremans, W. Wangermez, J. Rongé and J. A. Martens, Demonstration of a three compartment solar electrolyser with gas phase cathode producing formic acid from CO_2 and water using Earth abundant metals, *Front. Chem. Eng.*, 2022, **4**, 1028811.
4 N. Kato, S. Mizuno, M. Shiozawa, N. Nojiri, Y. Kawai, K. Fukumoto, T. Morikawa and Y. Takeda, A large-sized cell for solar-driven CO_2 conversion with a solar-to-formate conversion efficiency of 7.2%, *Joule*, 2021, **5**, 687–705.
5 N. Kato, Y. Kawai, N. Nojiri, M. Shiozawa, Y. Kikuzawa, N. Suzuki, S. Kosaka, Y. Kato, J. Seki, T. Hamaguchi and Y. Takeda, Enhancing Long-Term Durability of Electrochemical Reactors Producing Formate from CO_2 and Water Designed for Integration with Solar Cells, *ACS Omega*, 2024, **9**, 11646–11657.
6 Z. N. Zahran, Y. Miseki, E. A. Mohamed, Y. Tsubonouchi, K. Makita, T. Sugaya, K. Sayama and M. Yagi, Perfect Matching Factor between a Customized Double-Junction GaAs Photovoltaic Device and an Electrolyzer for Efficient Solar Water Splitting, *ACS Appl. Energy Mater.*, 2022, **5**, 8241–8253.
7 J. L. White, J. T. Herb, J. J. Kaczur, P. W. Majsztrik and A. B. Bocarsly, Photons to formate: Efficient electrochemical solar energy conversion via reduction of carbon dioxide, *J. CO_2 Util.*, 2014, **7**, 1–5.
8 M. C. Sauer, P. F. Southwick, K. S. Spiegler and M. R. J. Wyllie, Electrical Conductance of Porous Plugs - Ion Exchange Resin-Solution Systems, *Ind. Eng. Chem.*, 1955, **47**, 2187–2193.
9 L. Alvarado and A. Chen, Electrodeionization: Principles, Strategies and Applications, *Electrochim. Acta*, 2014, **132**, 583–597.
10 B. Zhang, H. Gao and Y. Chen, Enhanced Ionic Conductivity and Power Generation Using Ion-Exchange Resin Beads in a Reverse-Electrodialysis Stack, *Environ. Sci. Technol.*, 2015, **49**, 14717–14724.
11 A. Mahmoud, L. Muhr, G. Grévillot, G. Valentin and F. Lapicque, Ohmic drops in the ion-exchange bed of

Open Access Article. Published on 20 March 2026. Downloaded on 4/10/2026 3:06:36 PM.
This article is licensed under a Creative Commons Attribution-NonCommercial 3.0 Unported Licence.

cationic electrodeionisation cells, *J. Appl. Electrochem.*, 2006, **36**, 277–285.
12 A. D. Kraus, in *Heat Transfer Handbook*, eds. A. Bejan and A. D. Kraus, Wiley, Hoboken, 2003, ch. 1, pp. 1–42.
13 H. Tian, F. Mancilla-David, K. Ellis, E. Muljadi and P. Jenkins, A cell-to-module-to-array detailed model for photovoltaic panels, *Sol. Energy*, 2012, **86**, 2695–2706.
14 H. Yang, J. J. Kaczur, S. D. Sajjad and R. I. Masel, Electrochemical conversion of CO_2 to formic acid utilizing Sustainion™ membranes, *J. CO_2 Util.*, 2017, **20**, 208–217.
15 H. Yang, J. J. Kaczur, S. D. Sajjad and R. I. Masel, Performance and long-term stability of CO_2 conversion to formic acid using a three-compartment electrolyzer design, *J. CO_2 Util.*, 2020, **42**, 101349.
16 C. Xia, P. Zhu, Q. Jiang, Y. Pan, W. Liang, E. Stavitski, H. N. Alshareef and H. Wang, Continuous production of pure liquid fuel solutions via electrocatalytic CO_2 reduction using solid-electrolyte devices, *Nat. Energy*, 2019, **4**, 776–785.
17 L. Fan, C. Xia, P. Zhu, Y. Lu and H. Wang, Electrochemical CO_2 reduction to high-concentration pure formic acid solutions in an all-solid-state reactor, *Nat. Commun.*, 2020, **11**, 3633.
18 C. Zhang, X. Hao, J. Wang, X. Ding, Y. Zhong, Y. Jiang, M.-C. Wu, R. Long, W. Gong, C. Liang, W. Cai, J. Low and Y. Xiong, Concentrated Formic Acid from CO_2 Electrolysis for Directly Driving Fuel Cell, *Angew. Chem., Int. Ed.*, 2024, **63**, e202317628.
19 J. W. Blake, J. T. Padding and J. W. Haverkort, Analytical modelling of CO_2 reduction in gas-diffusion electrode catalyst layers, *Electrochim. Acta*, 2021, **393**, 138987.
20 C. T.-C. Wan, K. V. Greco, A. Alazmi, R. M. Darling, Y.-M. Chiang and F. R. Brushett, Methods-a potential-dependent thiele modulus to quantify the effectiveness of porous electrocatalysts, *J. Electrochem. Soc.*, 2021, **168**, 123503.
21 J. N. Schwämmlein, N. L. T. Pham, T. Mittermeier, M. Egawa, L. Bonorand and H. A. Gasteiger, Through-Plane Conductivity of Anion Exchange Membranes at Sub-Freezing Temperatures—Hydroxide *vs.* (Bi-)Carbonate Ions, *J. Electrochem. Soc.*, 2020, **167**, 084513.
22 J. R. Thome, in *Heat Transfer Handbook*, eds. A. Bejan and A. D. Kraus, Wiley, Hoboken, 2003, ch. 9, pp. 635–718.

 © 2026 The Author(s). Published by the Royal Society of Chemistry